



Waveguide asymmetric long-period grating couplers as refractive index sensors

JENS HØVIK, *  MUKESH YADAV, JONG WOOK NOH, AND ASTRID AKSNES

Norwegian University of Science and Technology, Department of Electronic Systems, Trondheim, Norway
*jens.hovik@ntnu.no

Abstract: A highly sensitive integrated photonic transducer is designed by utilizing asymmetric long-period gratings on a silicon waveguide. These gratings are formed by periodic perturbation of the waveguide width, leading to coupling between the fundamental mode and the 1st order asymmetric leaky mode. The coupled modes are studied via finite-element and finite-difference time-domain methods. Only a single fabrication step is required to realize this novel design. The device is utilized as a refractive index sensor in liquid, yielding a sensitivity of 5078 nm/RIU. The design is a unique combination of being highly sensitive, easily fabricated and highly compact.

© 2020 Optical Society of America under the terms of the [OSA Open Access Publishing Agreement](#)

1. Introduction

Over recent years an abundance of refractive index sensors has been developed in the field of integrated photonics. These sensors often function by evanescent field sensing with a sensitivity which directly correlates to the magnitude of the evanescent field of the guided mode. Each transducer design has advantages and disadvantages. Integrated photonic Mach-Zehnder interferometers (MZIs), for example, utilize an intensity-based sensing scheme where interference is caused by a relative phase shift between the two arms of the sensor. In spite of high sensitivity [1–3], MZIs have issues with signal ambiguity, proper balancing between sensing and reference arms, and relatively large size. In addition, conventional MZIs require real time monitoring of the signal. Other frequently used sensing mechanisms are resonance effects, such as ring resonators [4,5] or photonic crystal cavity resonators [6,7]. Optical ring resonators are several orders of magnitude more compact than MZIs and can be more easily multiplexed as they do not require continuous measurement of the transduction signal. The downsides are that the sensitivity is lower and the need to scan over a wavelength range.

Important performance indicators for transducers include limit of detection, dynamic range, sensor footprint, response time and selectivity. The definition of sensitivity will vary with the transducer design, but for resonator-based components it is generally defined as $\Delta\lambda/\Delta n$, indicating a shift in the resonance wavelength divided by the refractive index change. The limit of detection (LOD) is given by the sensor resolution R_λ divided by the sensitivity, S . It is common to approximate R_λ as three times the root-mean square of the total noise levels of the sensor [8]

$$LOD = \frac{R_\lambda}{S} \approx \frac{3\sigma}{S}. \quad (1)$$

For optical fiber-based sensors, one popular design is long-period perturbations of the fiber refractive index which was first introduced by Vengsarkar et al. [9]. Such a long-period grating (LPG) allows phase matching between the fundamental mode of the fiber and the cladding mode. LPGs have seen vast use in fiber-based sensors, ranging from structural to biomedical [10–13], and have just recently seen use in integrated photonics. In 2013 Liu et al. conducted a theoretical analysis on using long-period gratings for grating assisted light couplers as refractive index sensors [14] and later reported an experimental verification in 2016 [15]. Light was coupled between two asynchronous silicon nitride waveguides by phase matching using long-period gratings etched into

the surface of one waveguide, achieving a sensitivity of 1970 nm/RIU. In this paper we present an integrated photonic component utilizing a long-period grating structure on the silicon-on-insulator (SOI) platform. Our aim is to simplify the design making fabrication easier and potentially mass producible with complementary metal-oxide-semiconductor (CMOS) fabrication while also increasing the device sensitivity. This device is then fabricated and experimentally verified as a refractive index sensor using saline solutions of increasing concentration.

2. Working principle

2.1. Coupling between asynchronous modes

Two modes can achieve complete power transfer through evanescent wave coupling if they possess sufficient phase synchronization. This effect is commonly used in directional couplers [16] and ring resonators [4,5]. As the propagation constants of two modes diverge the phase synchronization between them decreases and the power transfer diminishes until no coupling occurs between the modes. Coupling between asynchronous modes is possible by utilizing gratings, which introduce a periodic perturbation in the waveguide. Close to the grating, a quasi-periodic mode distribution (or Bloch-waves) will be generated consisting of a set of spatial harmonics with propagation constants given by [17]

$$\beta_v = \beta_0 + m \frac{2\pi}{\Lambda}, \quad (2)$$

where β_v is the modified propagation constant, β_0 is the propagation constant of an unperturbed waveguide and Λ is the grating period. There exist multiple solutions to this equation as waves are periodic, indicated by the mode number, m . Coupling between two modes will occur when the modified propagation constant (Eq. (2)) of one mode matches the propagation constant of the second mode. Given two modes with propagation constants β_1 and β_2 , phase matching occurs when

$$\beta_1 - \beta_2 = m \frac{2\pi}{\Lambda}. \quad (3)$$

The equation for the grating period can thus be expressed as

$$\Lambda = \frac{\lambda}{n_{eff1} - n_{eff2}}, \quad (4)$$

where λ is the wavelength at which coupling occurs, and n_{eff1} and n_{eff2} are the effective refractive indices of the guided modes.

2.2. Coupling strength

The coupling coefficient between modes is given as a function of the mode overlap in the grating area [18]

$$\kappa = \frac{2c\epsilon_0}{\lambda} (n_c^2 - n_{cl}^2) \int_{\frac{w}{2}-d_c/2}^{\frac{w}{2}+d_c/2} u_1(x) \cdot u_2(x) dx. \quad (5)$$

Here d_c is the depth of the sidewall grating, w is the waveguide width, n_c and n_{cl} are the refractive indices of the core and cladding respectively, u_1 and u_2 are the field distributions of the two guided modes, c is the speed of light and ϵ_0 is the vacuum permittivity. Equation (5) calculates the coupling coefficient of a slab waveguide with a grating as shown in Fig. 1. For a three-dimensional

strip waveguide the equation becomes

$$\kappa = \frac{2c\epsilon_0}{\lambda} (n_c^2 - n_{cl}^2) \iint_A u_1 \cdot u_2 dA. \quad (6)$$

Here A is the grating area in a cross-section view, and u_1 and u_2 are normalized so that for each mode we have

$$\iint_{-\infty}^{\infty} E \times H^* = 1, \quad (7)$$

where E is the electric field and H is the magnetic field.

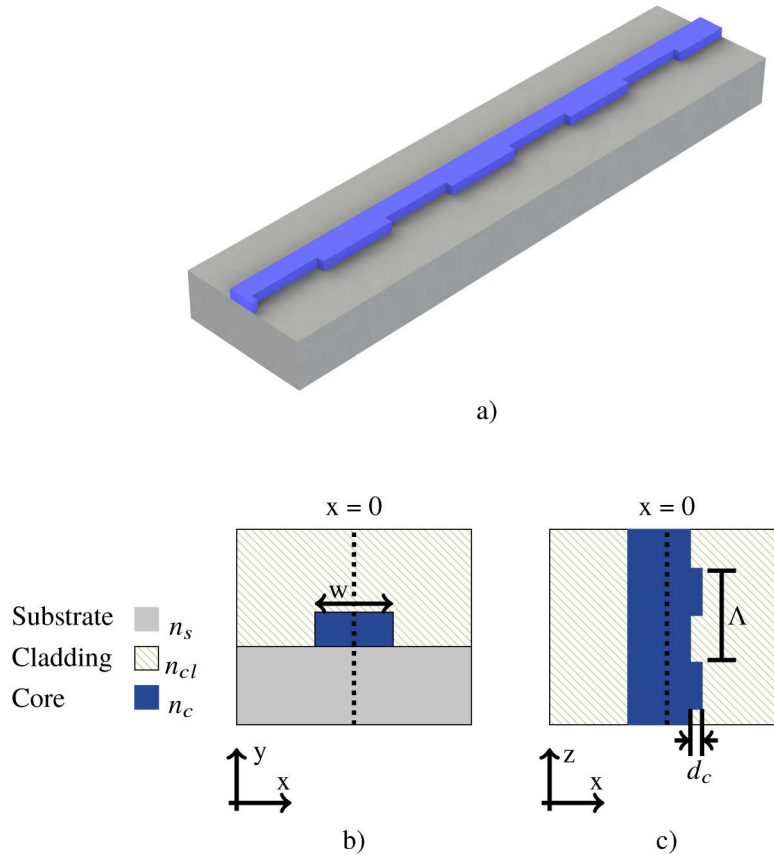


Fig. 1. (a) 3D model of slab waveguide with a long-period grating. (b) Cross section of waveguide. (c) Birds-eye view of waveguide with a long-period grating. w is the waveguide width, Λ is the grating period and d_c is the grating depth.

The derivation of Eq. (2) assumes the refractive index perturbation to be small in order to obtain its solution. As the refractive index difference between materials in silicon photonics is typically large (air/water to silicon), the grating equation may not be exact for all geometries. The grating depth is therefore kept much smaller than the propagation wavelength such that the relative perturbation of the guided mode is kept small and the assumptions required for Eq. (2) are still satisfied.

2.3. Coupler design

To simplify fabrication the gratings of the device are formed on the sidewall of the propagation waveguide. The gratings can then be defined in the lithography mask, making it possible to

fabricate the component in a single lithography and etch step. Only one waveguide is utilized and light is coupled from the fundamental TE-mode to a higher order radiated mode.

The starting point for the component design utilizes a well known device geometry for silicon strip waveguides, with a width of 500 nm, a waveguide height of 220 nm and a central wavelength of 1.55 μm . This particular design is chosen as a combination of low losses due to sidewall roughness, single-mode operation and low propagation losses in silicon [19]. The effective indices of the silicon (core), silicon oxide (substrate) and the water (cladding) used in the simulations are 3.47, 1.44 and 1.31, respectively. The required grating period can be found from Fig. 2 which shows the dispersion relation of a 500 nm \times 220 nm waveguide on silicon dioxide. The dispersion diagram shows the relationship between the frequency of a guided mode and its propagation constant. The effective index of the guided mode can then be calculated by using the formula

$$n_{\text{eff}} = \frac{c\beta}{f}, \quad (8)$$

where c is the speed of light, f is the frequency (y-axis of Fig. 2) and β is the propagation constant (x-axis of Fig. 2). The area above the lightline (shaded area in the figure) signifies the propagation constants of unbounded waves which will not propagate in the waveguide core. In these simulations water is chosen as the cladding material due to its relevance for biosensor applications. The required grating period to achieve coupling between two modes at a specific frequency can be calculated by first finding the propagation constants of the two modes from the dispersion relation. The wavelength $\lambda = 1.55 \mu\text{m}$ corresponding to a frequency of 193.54 THz is indicated in Fig. 2 to make it easier to find the correct parameters at this wavelength. By measuring the intersection of this frequency line with the two first TE-modes their respective propagation constants are found and Eq. (4) can be used to calculate the required period at this wavelength. At this grating period, coupling will occur between the fundamental TE mode and a mode unbounded by the waveguide core above the lightline, leading to a leaky mode which will be attenuated.

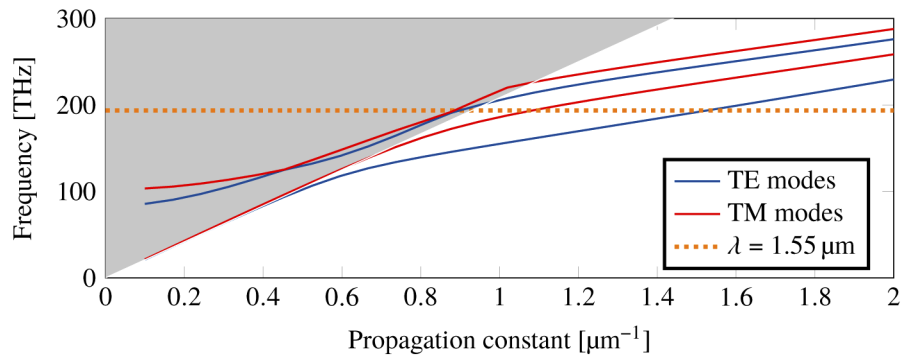


Fig. 2. Dispersion relation of a 500 nm \times 220 nm silicon waveguide on silicon dioxide in water. The two first modes for both TE and TM polarization are included. The orange line indicates the propagation constants at $\lambda = 1.55 \mu\text{m}$. The shaded area indicates the set of unbound frequencies above the lightline, which cannot propagate in the waveguide core.

The required grating length (corresponding to the number of periods times the grating period Λ) will depend on the coupling coefficient which can be calculated by Eq. (6). The number of periods can be controlled by the grating etch depth d_c . A high coupling coefficient enables a shorter coupling section, but a high field strength at the grating boundary will lead to increased losses. The losses associated with these gratings are therefore studied in section 4.1. Another notable feature of the sensor design is that there are only gratings on one side of the waveguide.

Utilizing asymmetric gratings is a quite common design in LPG fiber-optic sensing, where symmetric gratings are required to couple to symmetric cladding modes, while asymmetric gratings are required to couple to asymmetric cladding modes [20–22]. A similar design utilizing asymmetric gratings to design a highly tunable filter has also been developed by Q. Liu et al. [23].

3. Sensitivity analysis

The sensitivity of the device can be found using Eq. (4) (see appendix A for the derivation)

$$S = \lambda \frac{\frac{dn_{eff1}}{dn_{cl}} - \frac{dn_{eff2}}{dn_{cl}}}{n_{g1} - n_{g2}}, \quad (9)$$

where $\frac{dn_{eff1}}{dn_{cl}}$ and $\frac{dn_{eff2}}{dn_{cl}}$ are the effective index responses to a change in the cladding material n_{cl} for the two modes, n_{g1} and n_{g2} are their group indices and λ is the central wavelength. As the denominator ($n_{g1} - n_{g2}$) approaches zero the sensitivity grows exponentially. The waveguide properties are investigated using the frequency-domain eigensolver MPB Photonic Bands [24].

The group indices of the two modes can be found directly from the slopes of their dispersion relations in Fig. 2, while the refractive index sensitivity requires a second simulation to find the change in propagation constant as a function of the cladding refractive index, n_{cl} . Equation (9) can then be solved to obtain the graph of the sensitivity as plotted in Fig. 3(a). The small discontinuity at $\lambda = 1.6 \mu\text{m}$ is caused by the crossing of the effective index of the 1st order TE- and TM-modes (visible in Fig. 2) which causes the simulation software to return the wrong values for their respective effective indices in this small region.

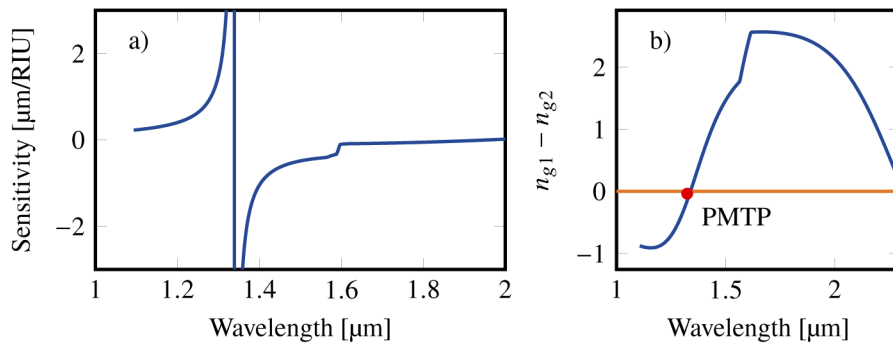


Fig. 3. a) The sensitivity of the long-period grating waveguide as a function of wavelength. At the asymptote around $\lambda = 1.35 \mu\text{m}$ the sensitivity is theoretically infinite. b) The difference in group index between the two guided modes. The crossing point of the group indices of these modes is the phase matching turning point (PMTP).

An asymptote with theoretically infinite sensitivity occurs around $\lambda = 1.35 \mu\text{m}$. This asymptote appears because the group index of the two modes have different wavelength dependencies, and as the wavelength is tuned they eventually become identical and the denominator in Eq. (9) becomes zero. The denominator of Eq. (9) is shown in Fig. 3(b). The denominator is zero at the phase matching turning point (PMTP). This effect has been significantly utilized in long-period fiber-optic sensors [25]. It is of interest to utilize this effect in integrated photonics where the fabrication is easier and the scale is much smaller than their fiber-optic counterparts [26–28]. Since Maxwell's equations are scale-invariant, the location of the PMTP can be tuned by varying the size of the waveguide.

4. Finite-difference time-domain simulations

The SOI long-period grating-coupler design is studied via the finite-difference time-domain (FDTD) method [29] using an open-source software package [30]. The required grating period at $\lambda = 1.55 \mu\text{m}$ can be found utilizing Eq. (4) in conjunction with Fig. 2, giving a required period of $1.59 \mu\text{m}$ for mode number 1 ($m = 1$). At short periodicities reflections between successive perturbations occur, causing interference and considerable wavelength-dependent losses and noise. Higher diffraction orders are therefore evaluated, as they were found to exhibit lower levels of noise. Figure 4 shows the simulated response of a $600 \mu\text{m}$ long waveguide with a 50 nm sidewall grating depth and a grating period of $8.1 \mu\text{m}$, corresponding to the fifth order diffraction mode. There is a dip in the transmission spectrum at $\lambda = 1.587 \mu\text{m}$. The distribution of the electromagnetic field in the waveguide is shown for two wavelengths, one wavelength corresponding to the phase matching condition while the other does not. At $\lambda = 1.49 \mu\text{m}$ the phase matching condition is not met and the field distribution is unchanged as the mode propagates (Fig. 4(b)). At $\lambda = 1.587 \mu\text{m}$ the phase condition is met and the field distribution tends to the asymmetric radiating mode (Fig. 4(c)).

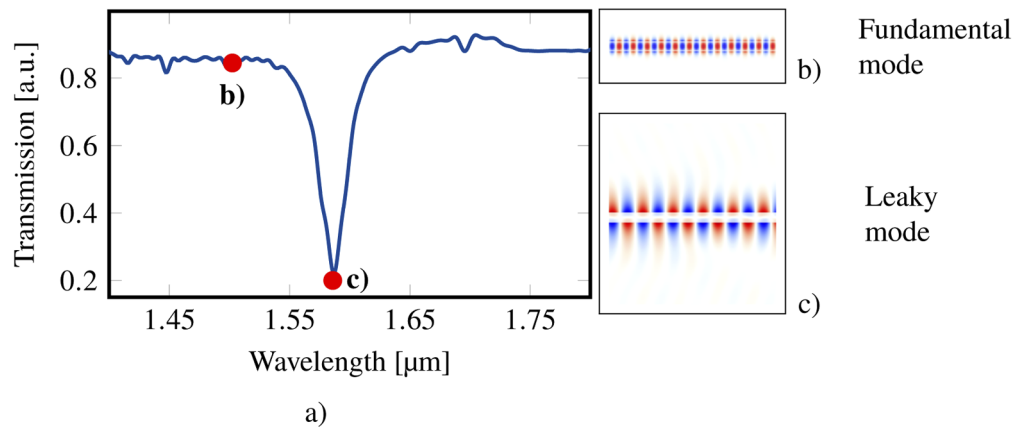


Fig. 4. a) Transmission through an asymmetrical waveguide with grating period $\Lambda = 8.1 \mu\text{m}$, grating length $600 \mu\text{m}$ and grating depth $d_c = 50 \text{ nm}$. The electromagnetic field profile after a propagation length equal to L_c b) not at the wavelength to achieve phase matching c) at the correct wavelength to achieve phase matching.

The working principle of the device is illustrated by the simulation of the waveguide at $\lambda = 1.55 \mu\text{m}$. However, at this wavelength the device is not operating at the PMTP where the sensitivity is highest. The PMTP is at $\lambda = 1.35 \mu\text{m}$ as can be seen in Fig. 3. To determine the PMTP, the wavelength area around $1.35 \mu\text{m}$ is investigated by altering the grating period Λ until the resonance dips occur at this wavelength range. The grating period is then increased in increments of $0.05 \mu\text{m}$ to show the evolution of the PMTP as the grating period is changing. The results are displayed in Fig. 5.

When the grating period is too low for coupling to occur at the phase match turning point there is no coupling and the transmission is constant over the wavelength range (Fig. 5(a)). As the grating period is increased the central coupling wavelength shifts and a broad intensity dip appears at the phase match turning point (Fig. 5(b)). Two distinct resonance effects appear and move in opposite directions as the grating period is increased ((Figs. 5(c) and (d)). The two resonances move in opposite directions because the sensitivity of the phase matching effect on each side of the PMTP have opposite signs, where one dip blue shifts with the refractive index change and the other red shifts.

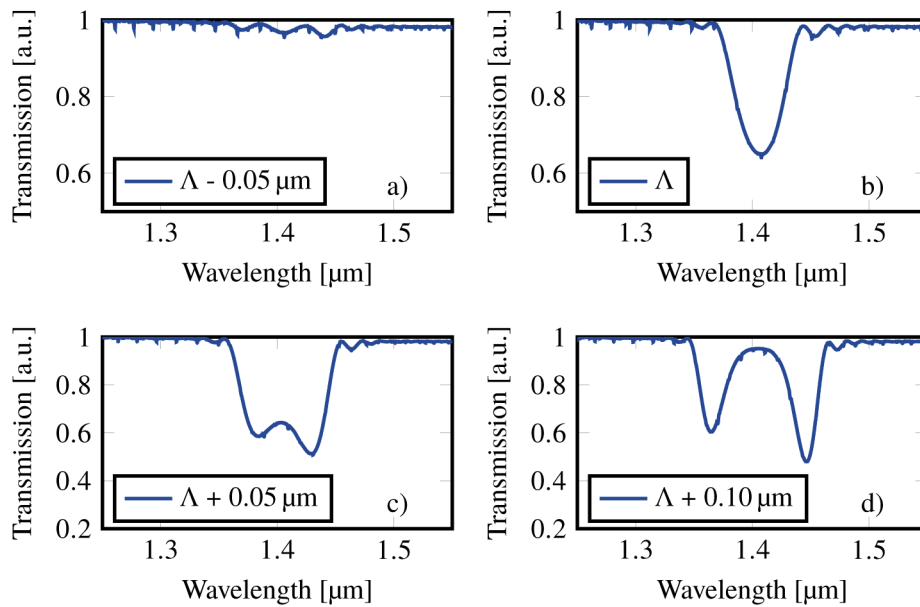


Fig. 5. Transmission near the phase match turning point as the grating period is varied around perfect matching. Λ here refers to the grating period which allows coupling at the phase match turning point.

To study the refractive index sensitivity of the design, the simulation parameters are chosen such that the device geometry operates close to the PMTP with both resonance dips visible. The results of this study are shown in Fig. 6 where the transmission as a function of wavelength and refractive index of the cladding material is plotted. For each iterative increase of the cladding refractive index the transmission dips move closer to the PMTP. From the figure it can be observed that the response to a change in refractive index is not linear but rather exponential. The result is in good agreement with Fig. 3(a) which shows the sensitivity as exponential close to the PMTP. The final iterative increase in the cladding refractive index gives a simulated sensitivity of 18 700 nm/RIU. As the refractive index of the cladding increases the two dips will eventually merge and the resonances disappear.

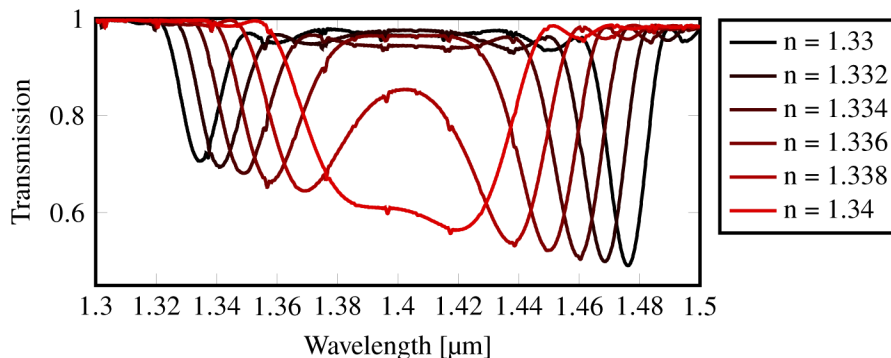


Fig. 6. Transmission as a function of wavelength while the refractive index of the cladding material increases from $n=1.33$ to $n=1.34$.

5. Experimental results

Test samples are fabricated in-house by growing hydrogenated amorphous silicon (α -Si:H) on top of silicon wafers with a 1 μm thick layer of thermally grown silicon dioxide (University Wafer). The waveguides are patterned using a 200 nm-thick layer of the positive e-beam resist CSAR6200 and an electron-beam lithography system (Elionix ELS-G100). The waveguides are patterned into the silicon layer using an inductively coupled plasma reactive-ion etching (ICP-RIE) system (Oxford Instruments) and a mixture of CHF_3 and SF_6 for an anisotropic and low-roughness etch. $2 \times 2 \mu\text{m}$ polymer waveguides are utilized as spot-size converters in conjunction with inverted silicon tapers. Coupling to the individual waveguides is performed using tapered lensed single-mode fibers with a beam spot-diameter of 2.5 μm (OZ-optics). The light source is a Thorlabs TLK-1550M Littman external cavity laser. Sample delivery to the transducers is performed via microfluidic channels made in polydimethylsiloxane (PDMS). The flow is controlled at a constant rate by utilizing Harvard Apparatus Pico Plus Elite syringe pumps. A schematic illustration of the characterization setup is shown in Fig. 7.

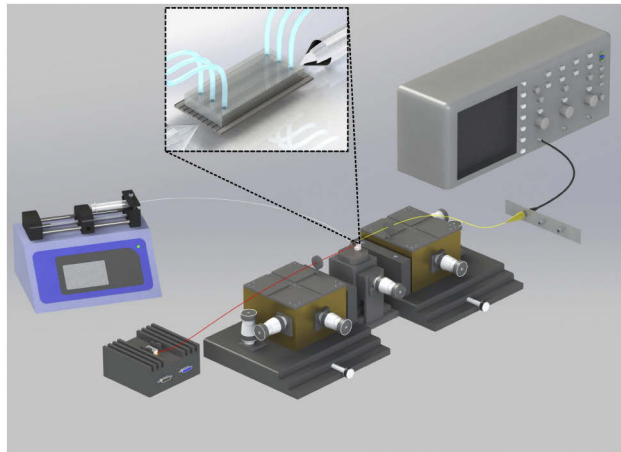


Fig. 7. A schematic illustration of the characterization setup including a syringe pump, a tunable laser, translation stages with tapered fibers for coupling to and from the chip, as well as a photodiode which translates the optical signal to an electrical signal. A Labview program is used to control the setup as well as for data acquisition and signal analysis.

5.1. Grating loss experiments

A long-period grating on a high refractive index-contrast waveguide will lead to scattering losses. These losses should be kept at a minimum in order to maximize the signal-to-noise ratio and thus the limit of detection of the device. Additionally, a low-loss transducer has a higher potential for multiplexing by using multiple long-period grating structures on a single input and output facet. Multiple loss-tests are therefore performed. Straight waveguides are fabricated with grating depths of 5 nm, 10 nm, 20 nm, 30 nm, 50 nm, and 100 nm. Such a waveguide with the 100 nm grating depth is displayed in Fig. 8(a). Three waveguides of each grating depth are fabricated for a total of 21 waveguides with 100 grating periods each. Due to the long coherence length of the external cavity laser, the total transmission at a specific wavelength can vary from waveguide to waveguide simply due to Fabry-Perot noise. The laser is therefore swept over a range of 100 nm to normalize the Fabry-Perot noise for each waveguide. The loss is found by comparing the total transmission for waveguides with and without gratings.

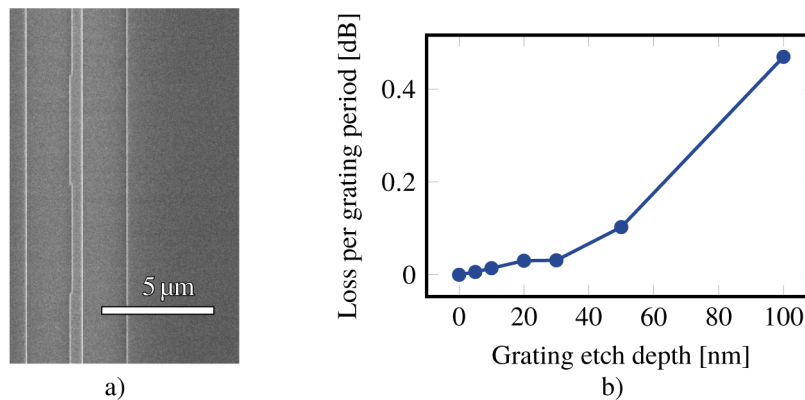


Fig. 8. a) SEM image of a waveguide with 100 nm grating etch depths b) Losses per grating period as a function of grating etch depth.

Figure 8(b) depicts the loss per grating period as a function of the grating etch depth. A grating depth of 5 nm gave losses as low as 0.006 dB per grating while still achieving coupling to the higher order asymmetric mode. Such narrow grating depths however required coupling sections longer than 3000 μm . As the grating depths increased in size the required transducers lengths grew shorter but as indicated by Fig. 8(b) the losses per grating grew exponentially. At 100 nm grating depth the losses were as high as 0.5 dB per grating. A 10 nm grating depth was found to give both low losses (~ 0.014 dB / period) and acceptable coupling lengths (~ 1500 μm for our design) and is thus the chosen grating depth.

5.2. Sensitivity tests

The sensitivity of a given device configuration is found by measuring the response of the device to a change in the refractive index of the surrounding cladding. This is performed by diluting salt in water to make various saline concentrations that comprises the cladding material. The chosen saline concentrations were 0%, 6%, 12% and 18% salt in water. To prevent congregation of salt on the sensor surface, deionized water was continuously flowed between measurements. The central resonance wavelength of the transmission dip (as can be seen in Fig. 9) is then tracked as a function of time, while the various saline concentrations are flowed across the sensor. This gives a sensitivity measurable in $\mu\text{m}/\text{RIU}$ (micrometer resonance shift divided by the change in refractive index unit). Since the sensitivity is seen to vary greatly with proximity to the PMTP (see Fig. 3), performing sensitivity tests for different geometries allows one to pinpoint the location of the PMTP where the sensitivity is the highest. Unlike the computational analysis, the experimental tests are limited to the tunable range of the laser source (1480 nm to 1620 nm). The PMTP is therefore found by altering the device geometry rather than tuning the grating period until the PMTP appears at the design wavelength. Fifteen waveguides of widths ranging from 450 nm to 600 nm are fabricated and the sensitivity of each design is found. The results are shown in Fig. 10. The sensitivity increases until the PMTP is found close to 1.55 μm at a waveguide width of 580 nm.

The transmission spectra for 0% and 6% solutions of saline for a device with the PMTP within the tunable range are shown in Fig. 11. For a 12% saline concentration the two resonance dips merged and their exact locations became difficult to determine. The distance between peaks for 0% and 6% is 109 nm and 56.7 nm, respectively. The refractive index of saline concentrations at 1550 nm is $1.3105 + 0.17152 * p\%$ [31] where p is the salt concentration. The calculated sensitivity is then 5078 nm/RIU. This is approximately 3-4 times lower than the sensitivity found

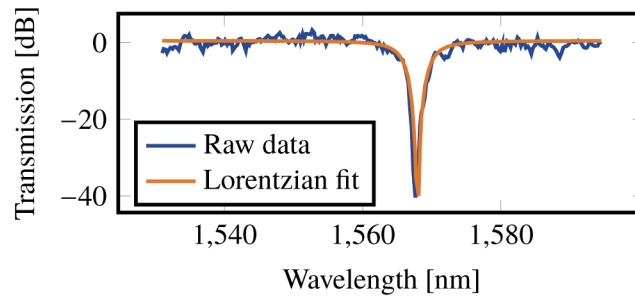


Fig. 9. Transmission through waveguide with a long-period grating. The dip in transmission at ~ 1570 nm is clearly visible. The LPG-coupler had a grating depth of 10 nm, grating periodicity of 7.8 μm and a grating length of 1500 μm .

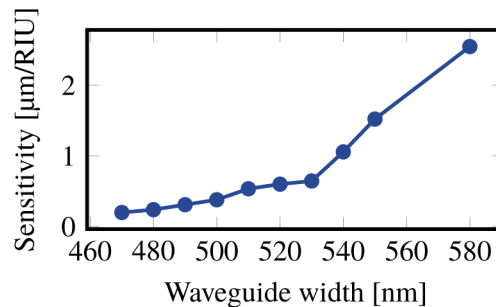


Fig. 10. Sensitivity as a function of waveguide width, corresponding to the distance from the phase match turning point. The waveguide height, grating depth and grating length are constant between measurements at 220 nm, 10 nm and 1500 μm , respectively.

in the FDTD-simulations in section 4. This is caused by the exponential change in sensitivity of the device close to the PMTP. It is difficult to engineer an experiment that measures the sensitivity just as the two resonance dips are about to merge. Determining the highest sensitivity is easier in a simulation environment where all material parameters are known and constant. The agreement between simulated and experimental results are otherwise good and within the expected fabrication tolerances of the device.

5.3. Noise

The LOD depends on how accurately the phase matching frequency can be determined. In Fig. 9 the full-width half-maximum (FWHM) is 4 nm. Equivalently a ring resonator was fabricated on the same chip in order to compare noise, yielding a FWHM of 200 pm in water. Tracing a single resonance point over time for both transducers gives a RMS noise level of 11.5 pm for the ring resonator and 37.5 pm for the grating coupler. The relationship between the FWHM of the resonator and the noise levels of the system is not linear. The accuracy to which one can determine the central point of a dip in transmission is governed by the noise levels of the system, the number of samples across the resonance and the quality of the Lorentzian curve-fitting which is used to determine the resonance central point. Most of these parameters do not change despite a larger FWHM. Although the grating coupler has a 20 times wider transmission dip, the noise levels increase by a factor 3. A narrower transmission peak is desirable, but the large increase in sensitivity from the grating coupler design offsets the noise factor.

When the long-period grating coupler approaches the PMTP, the waveguide becomes multimode as the 1st order TE-mode crosses the light line. This leads to wavelength-dependent interference

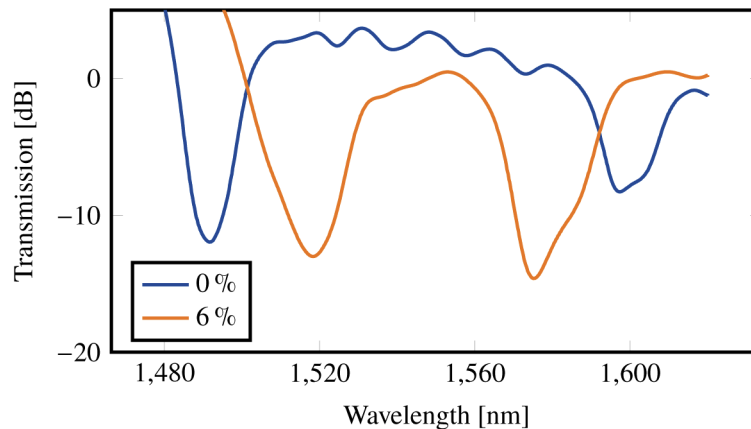


Fig. 11. Transmission near the PMTP for two different saline concentrations. The resonance dips experience significant broadening around the PMTP because the group indices match so a larger distribution of wavelengths satisfy the phase matching condition.

in the waveguide. As a result, the noise levels increase when the waveguide geometry is tuned to the PMTP. The graph in Fig. 11 has been fitted via a smoothing spline fit, using a piecewise polynomial fit to remove multimode interference noise inside the resonances.

6. Discussion

Our waveguide asymmetric long-period grating exhibits high sensitivities for multiple design parameters, with the highest achievable sensitivities occurring close to the PMTP, where a sensitivity of 5078 nm/RIU is measured. This is 2.5 times enhanced over the sensitivity achieved by Liu et al., while also having a simple design geometry. A typical race-track ring-resonator design in comparison has a sensitivity of ~ 70 nm/RIU [32]. For ring resonators the sensitivity can be increased further by maximizing the overlap between the electromagnetic field with the surrounding material. Flueckiger et al. have shown that by utilizing sub-wavelength gratings the ring-resonator sensitivity can be increased to 490 nm/RIU [33].

Due to the exponential sensitivity close to the PMTP, our device needs to be carefully designed to function optimally. A possible improvement of the device is to extend the sensitivity around the PMTP by tuning the design such that the matching of the two group indices occurs over a longer wavelength range (i.e. having group indices with more matched slopes at their intersection). Additionally, the noise of the system can be reduced further by increasing the coupling coefficient leading to a lower FWHM of the coupling, which makes determination of the central coupling wavelength easier. Reduction of multimode noise can also be achieved with a design that allows coupling between the fundamental and higher order modes without resorting to a multimode geometry. Alternatively, multimode noise can be reduced by waveguide tapering or on-chip mode demultiplexing. Although both simulations and experimental measurements utilize water as the cladding material the device is fully capable of operating with different refractive index claddings such as polymers, air or other gas compositions. Changing the cladding material will shift the PMTP, and the operating wavelength or the transducer design must be changed accordingly.

7. Conclusion

We designed, fabricated and characterized waveguide asymmetric long-period grating couplers as refractive index sensors on the silicon-on-insulator platform. The design shows increasing sensitivity as the device geometry is tuned such that the resonance occurs closer to the PMTP.

The fabricated and experimentally verified component exhibits a high sensitivity of 5078 nm/RIU at the phase-matching turning point. For use in high-density integrated photonics the losses of the design are also considered and minimized by finding the minimal grating depth for successful coupling of light between modes. For 5 nm grating depths, the losses were measured as low as 0.006 dB per grating period, without impacting coupler functionality. The sensor has the ability to be a unique combination of highly compact, easy to fabricate and highly sensitive compared to many other transducer designs.

Appendix A: derivation of the sensitivity formula

Begin by considering the grating equation, i.e.

$$\Lambda = \frac{\lambda}{n_1 - n_2}, \quad (10)$$

where n_1 and n_2 are the effective indices of the first and second guided mode. For a fabricated component that undergoes a shift in the refractive index of the cladding the formula before and after the shift are

$$\Lambda = \frac{\lambda_1}{n_1 - n_2}, \quad (11)$$

and

$$\Lambda = \frac{\lambda_2}{n_{1s} - n_{2s}}. \quad (12)$$

where n_{1s} and n_{2s} are the effective indices of the guided mode after the refractive index of the cladding has changed. These indices are a function of both the refractive index of the surrounding cladding but also as a function of the corresponding shift in the resonance wavelength λ , i.e.:

$$n_{xs} = n_x + \Delta n \frac{\delta n_x}{\delta n} + \Delta \lambda \frac{\delta n_x}{\delta \lambda}. \quad (13)$$

The grating period Λ does not change, and consequently the two equations are equal which gives

$$\frac{\lambda_1}{n_1 - n_2} = \frac{\lambda_2}{n_1 + \Delta n \frac{\delta n_1}{\delta n} + \Delta \lambda \frac{\delta n_1}{\delta \lambda} - \left(n_2 + \Delta n \frac{\delta n_2}{\delta n} + \Delta \lambda \frac{\delta n_2}{\delta \lambda} \right)}. \quad (14)$$

This can be rewritten as

$$\lambda_1 \left(n_1 + \Delta n \frac{\delta n_1}{\delta n} + \Delta \lambda \frac{\delta n_1}{\delta \lambda} - \left(n_2 + \Delta n \frac{\delta n_2}{\delta n} + \Delta \lambda \frac{\delta n_2}{\delta \lambda} \right) \right) = \lambda_2 (n_1 - n_2). \quad (15)$$

Extracting the three variables $n_1 - n_2$, Δn and $\Delta \lambda$ yields

$$\lambda_1 (n_1 - n_2) + \lambda_1 \Delta n \left(\frac{\delta n_1}{\delta n} - \frac{\delta n_2}{\delta n} \right) + \lambda_1 \Delta \lambda \left(\frac{\delta n_1}{\delta \lambda} - \frac{\delta n_2}{\delta \lambda} \right) = \lambda_2 (n_1 - n_2), \quad (16)$$

and since $\lambda_1 - \lambda_2 = \Delta \lambda$ the equation can be simplified as

$$\Delta \lambda \left(n_1 - n_2 + \lambda_1 \left(\frac{\delta n_1}{\delta \lambda} - \frac{\delta n_2}{\delta \lambda} \right) \right) = \lambda_1 \Delta n \left(\frac{\delta n_1}{\delta n} - \frac{\delta n_2}{\delta n} \right). \quad (17)$$

Dividing by Δn gives

$$\frac{\Delta \lambda}{\Delta n} \left(n_1 - n_2 + \lambda_1 \left(\frac{\delta n_1}{\delta \lambda} - \frac{\delta n_2}{\delta \lambda} \right) \right) = \lambda_1 \left(\frac{\delta n_1}{\delta n} - \frac{\delta n_2}{\delta n} \right). \quad (18)$$

$\frac{\Delta\lambda}{\Delta n}$ is the definition of the sensitivity so the equation can be solved to get

$$S = \frac{\lambda_1 \left(\frac{\delta n_1}{\delta n} - \frac{\delta n_2}{\delta n} \right)}{\left(n_1 - n_2 + \lambda_1 \left(\frac{\delta n_1}{\delta \lambda} - \frac{\delta n_2}{\delta \lambda} \right) \right)}. \quad (19)$$

Since

$$n_g = n + \lambda \frac{\delta n}{\delta \lambda}, \quad (20)$$

the denominator can be simplified to obtain the sensitivity of the long-period grating sensor as

$$S = \lambda \frac{\frac{dn_1}{dn} - \frac{dn_2}{dn}}{n_{g1} - n_{g2}}. \quad (21)$$

Funding

Norges Forskningsråd (245963/F50, 248869/O70).

Acknowledgments

We acknowledge the Norwegian University of Science and Technology for funding the PhD scholarship in Biotechnology and the Research Council of Norway for funding the Lab-on-a-chip Biophotonic Sensor Platform for Diagnostics project (project number 248869/O70) and for their support to the Norwegian Micro- and Nano-Fabrication Facility, NorFab, project number 245963/F50.

Disclosures

The authors declare no conflicts of interest.

References

1. V. Ahsani, F. Ahmed, M. Jun, and C. Bradley, "Tapered fiber-optic mach-zehnder interferometer for ultra-high sensitivity measurement of refractive index," *Sensors* **19**(7), 1652–1662 (2019).
2. X. Jiang, Y. Chen, F. Yu, L. Tang, M. Li, and J.-J. He, "High-sensitivity optical biosensor based on cascaded mach-zehnder interferometer and ring resonator using vernier effect," *Opt. Lett.* **39**(22), 6363–6366 (2014).
3. B. Sepulveda, J. S. del Rio, M. Moreno, F. J. Blanco, K. Mayora, C. Dominguez, and L. M. Lechuga, "Optical biosensor microsystems based on the integration of highly sensitive mach-zehnder interferometer devices," *J. Opt. A: Pure Appl. Opt.* **8**(7), S561–S566 (2006).
4. M. Iqbal, M. A. Gleeson, B. Spaugh, F. Tybor, W. G. Gunn, M. Hochberg, T. Baehr-Jones, R. C. Bailey, and L. C. Gunn, "Label-Free Biosensor Arrays Based on Silicon Scanning Instrumentation," *IEEE J. Sel. Top. Quantum Electron.* **16**(3), 654–661 (2010).
5. L. Vivien, D. Marris-Morini, A. Griol, K. B. Gylfason, D. Hill, J. Lvarez, H. Sohlström, J. Hurtado, D. Bouville, and E. Cassan, "Vertical multiple-slot waveguide ring resonators in silicon nitride," *Opt. Express* **16**(22), 17237–17242 (2008).
6. K. H. Hwang and G. H. Song, "Design of a high-Q channel add-drop multiplexer based on the two-dimensional photonic-crystal membrane structure," *Opt. Express* **13**(6), 1948–1957 (2005).
7. Z. Zhang and M. Qiu, "Compact in-plane channel drop filter design using a single cavity with two degenerate modes in 2D photonic crystal slabs," *Opt. Express* **13**(7), 2596–2604 (2005).
8. I. M. White and X. Fan, "On the performance quantification of resonant refractive index sensors," *Opt. Express* **16**(2), 1020–1028 (2008).
9. A. M. Vengsarkar, P. J. Lemaire, J. B. Judkins, V. Bhatia, T. Erdogan, and J. E. Sipe, "Long-period fiber gratings as band rejection filters," *J. Lightwave Technol.* **14**(1), 58–65 (1996).
10. L. Alwis, T. Sun, and K. T. Grattan, "[INVITED] Developments in optical fibre sensors for industrial applications," *Opt. Laser Technol.* **78**, 62–66 (2016).
11. R. Correia, S. James, S. W. Lee, S. P. Morgan, and S. Korposh, "Biomedical application of optical fibre sensors," *J. Opt.* **20**(7), 073003 (2018).
12. M. Ramakrishnan, G. Rajan, Y. Semenova, and G. Farrell, "Overview of fiber optic sensor technologies for strain/temperature sensing applications in composite materials," *Sensors* **16**(1), 99 (2016).

13. L. Mescia and F. Prudenzano, "Advances on optical fiber sensors," *Fibers* **2**(1), 1–23 (2013).
14. Q. Liu, J. S. Kee, and M. K. Park, "A refractive index sensor design based on grating-assisted coupling between a strip waveguide and a slot waveguide," *Opt. Express* **21**(5), 5897–5909 (2013).
15. Q. Liu, Z. Gu, M. K. Park, and J. Chung, "Experimental demonstration of highly sensitive optical sensor based on grating-assisted light coupling between strip and slot waveguides," *Opt. Express* **24**(12), 12549–12556 (2016).
16. W. K. Burns, A. F. Milton, A. B. Lee, and E. J. West, "Optical mode evolution 3-db coupler," *Appl. Opt.* **15**(4), 1053–1065 (1976).
17. P. K. Tien, "Light waves in thin films and integrated optics," *Appl. Opt.* **10**(11), 2395–2413 (1971).
18. D. Marcuse, "Directional couplers made of nonidentical asymmetric slabs. Part I: Synchronous couplers," *J. Lightwave Technol.* **5**(1), 113–118 (1987).
19. L. Chrostowski and M. Hochberg, *Silicon Photonics Design: From Devices to Systems* (Cambridge University, 2015).
20. J. N. Blake, B. Y. Kim, H. E. Engan, and H. J. Shaw, "Analysis of intermodal coupling in a two-mode fiber with periodic microbends," *Opt. Lett.* **12**(4), 281–283 (1987).
21. I. K. Hwang, S. H. Yun, and B. Y. Kim, "Long-period fiber gratings based on periodic microbends," *Opt. Lett.* **24**(18), 1263–1265 (1999).
22. G. Rego, O. V. Ivanov, and P. V. S. Marques, "Demonstration of coupling to symmetric and antisymmetric cladding modes in arc-induced long-period fiber gratings," *Opt. Express* **14**(21), 9594–9599 (2006).
23. Q. Liu, Z. Gu, J. S. Kee, and M. K. Park, "Silicon waveguide filter based on cladding modulated anti-symmetric long-period grating," *Opt. Express* **22**(24), 29954–29963 (2014).
24. S. Johnson and J. Joannopoulos, "Block-iterative frequency-domain methods for Maxwell's equations in a planewave basis," *Opt. Express* **8**(3), 173–190 (2001).
25. M. Partridge, R. Wong, S. W. James, F. Davis, S. P. J. Higson, and R. P. Tatam, "Long period grating based toluene sensor for use with water contamination," *Sens. Actuators, B* **203**, 621–625 (2014).
26. A. Martinez-Rios, D. Monzon-Hernandez, I. Torres-Gomez, and G. Salceda-Delgado, "Long period fibre gratings," in *Fiber Optic Sensors*, M. Yasin, H. Arof, and S. W. Harun, eds. (Intech Open, 2012), chap. 11, pp. 275–294.
27. R. Y. N. Wong, E. Chehura, S. E. Staines, S. W. James, and R. P. Tatam, "Fabrication of fiber optic long period gratings operating at the phase matching turning point using an ultraviolet laser," *Appl. Opt.* **53**(21), 4669–4674 (2014).
28. T. Mizunami and T. Fukuda, "FEM calculation and the effects of hydrogen diffusion in fabrication processes of long-period fiber gratings," *Opt. Commun.* **259**(2), 581–586 (2006).
29. A. Taflov and S. Hagness, *Computational Electrodynamics: The Finite-Difference Time-Domain Method*, 3rd edition., vol. 2062 (Artech House, 2005).
30. A. F. Oskooi, D. Roundy, M. Ibanescu, P. Bermel, J. D. Joannopoulos, and S. G. Johnson, "Meep: A flexible free-software package for electromagnetic simulations by the FDTD method," *Comput. Phys. Commun.* **181**(3), 687–702 (2010).
31. H. Su and X. G. Huang, "Fresnel-reflection-based fiber sensor for on-line measurement of solute concentration in solutions," *Sens. Actuators, B* **126**(2), 579–582 (2007).
32. K. De Vos, I. Bartolozzi, E. Schacht, P. Bienstman, and R. Baets, "Silicon-on-Insulator microring resonator for sensitive and label-free biosensing," *Opt. Express* **15**(12), 7610–7615 (2007).
33. J. Flueckiger, S. Schmidt, V. Donzella, A. Sherwali, D. M. Ratner, L. Chrostowski, and K. C. Cheung, "Sub-wavelength grating for enhanced ring resonator biosensor," *Opt. Express* **24**(14), 15672–15686 (2016).